Article

A Deep Learning Strategy for the Retrieval of Sea Wave Spectra from Marine Radar Data

Giovanni Ludeno [1], Giuseppe Esposito [1,*], Claudio Lugni [2], Francesco Soldovieri [1] and Gianluca Gennarelli [1]

[1] Institute for Electromagnetic Sensing of the Environment, National Research Council of Italy, Via Diocleziano 328, 80124 Napoli, Italy; ludeno.g@irea.cnr.it (G.L.); soldovieri.f@irea.cnr.it (F.S.); gennarelli.g@irea.cnr.it (G.G.)

[2] Institute of Marine Engineering, National Research Council of Italy, Via di Vallerano 139, 00128 Rome, Italy; claudio.lugni@cnr.it

* Correspondence: esposito.g@irea.cnr.it

Abstract: In the context of sea state monitoring, reconstructing the wave field and estimating the sea state parameters from radar data is a challenging problem. To reach this goal, this paper proposes a fully data-driven, deep learning approach based on a convolutional neural network. The network takes as input the radar image spectrum and outputs the sea wave directional spectrum. After a 2D fast Fourier transform, the wave elevation field is reconstructed, and accordingly, the sea state parameters are estimated. The reconstruction strategy, herein presented, is tested using numerical data generated from a synthetic sea wave simulator, considering the spectral proprieties of the Joint North Sea Wave Observation Project model. A performance analysis of the proposed deep-learning estimation strategy is carried out, along with a comparison to the classical modulation transfer function approach. The results demonstrate that the proposed approach is effective in reconstructing the directional wave spectrum across different sea states.

Keywords: marine radar; U-NET; sea wave spectra; sea state estimation

1. Introduction

The observation of sea wave motion and the accurate characterization of sea state parameters provide valuable information for safety, navigation, coastal management, offshore operations, environmental monitoring, and resource management. In this framework, microwave radar systems have proven to be effective for measuring the wave spectra and retrieving the sea state information, both offshore and nearshore, with a high spatial and temporal resolution [1,2]. Radar systems are usually classified according to the operating frequency, and the bands adopted for sea state monitoring range from UHF (0.3–1 GHz) to Ka (26.5–40 GHz) bands [3–9]. The choice of the frequency band depends on the application requirements and has a notable impact on the sensing capabilities and installation flexibility.

In the last decades, Marine Radar (MR), mostly operating at X-band (8–12 GHz), has received considerable interest in the context of sea state monitoring or retrieving the sea state information in a range of a few kilometers from the observation platform [4]. Depending on the type of data, MRs can be classified into two categories: non-coherent and coherent radars. The first one only measures the amplitude of the electromagnetic signal reflected by the marine surface (herein considered), while the second one measures both amplitude and phase information [10].

A specific radar data processing is required to retrieve the information about the sea state. Currently, well-assessed procedures are available in the literature [11,12], which allow retrieving the hydrographic parameters of the wave motion, such as wavelength (λ_p), period (T_p), and direction (θ_p) of the dominant wave; the significant wave height (H_s); as well as the sea surface current and bathymetry fields with high accuracy. The basic

steps of a typical sea state estimation procedure for a non-coherent MR can be summarized as follows:

- A 3D fast Fourier transform (FFT) is performed to convert the MR image sequence from a space–time domain to a wavenumber–frequency one;
- A band-pass filter is applied to the radar image spectrum based on the dispersion relation describing the gravity sea waves;
- A modulation transfer function (MTF) permits to compensate the spectral distortion introduced by the radar-sensing process and converts the radar image spectrum into a sea spectrum;
- The sea surface elevation is reconstructed in the space–time domain via an inverse 3D Fourier transform (IFFT) of the sea spectrum achieved in the previous step.

A crucial point in the above data processing chain is the determination of the MTF because the modulation phenomena affect the radar sensing principle (e.g., tilt modulation and shadowing). These phenomena depend on the sea state, radar parameters (e.g., the space–time resolution of radar data), as well as on the acquisition geometry (e.g., antenna height). As a result, radar images do not reproduce the sea surface elevation [11,13–15]. Therefore, the role played by MTF is crucial in compensating the modulation effects and retrieving the sea surface elevation profile. In this context, the empirical methods based on linear fitting [11], polynomial fitting [16], and linear fitting with variable exponent [17] have been proposed in the literature for the MTF evaluation. The MTFs were determined by analyzing marine radar measurements and in situ buoy observations in deep water. Specifically, the MTFs were fit to a power decay law of wavenumbers by using 1D wavenumber spectrum from marine radar and buoy measurements.

Although these techniques work well for sea states with a strongly dominant wave direction and narrow directional spreading, the angular dependence of the wave spectrum is overlooked. Based on these considerations, a directional MTF has been recently introduced in [18]. It should also be stressed that the quality of the directional spectrum reconstruction impacts not only the sea surface reconstruction but also the estimation of the sea state parameters such as H_s, T_p, and λ_p. For this reason, many researchers have focused on the estimation of these parameters, bypassing the calibration of the image radar spectrum.

The significant wave height, which is one of the most important parameters for sea state monitoring, has been estimated by taking into account the correlation between the sea surface elevation and the shadowing phenomenon [19–22] or by exploiting artificial intelligence approaches [23–28]. The latter includes support vector regression-based methods [23,24], multilayer perceptrons [25], and a convolutional neural network (CNN)-based method [26–28]. In addition, a CNN-based method has been recently adopted for the sea surface reconstruction [29].

In this paper, we investigate the possibility of retrieving the directional wave spectrum and, consequently, the sea state parameters and sea surface elevation by using the popular U-NET architecture (e.g., see [30–33]). The feasibility of this approach is validated through a numerical analysis featuring a wide dataset accounting for different sea conditions. A synthetic sea wave simulator was developed by applying the Fourier domain approach [34–36] and considering the spectral proprieties of the Joint North Sea Wave Observation Project (JONSWAP) model [37]. For each sea wave realization, the corresponding radar image was generated by taking into account the different known mechanisms responsible for the backscattering phenomenon of the electromagnetic fields transmitted by the radar antenna [11,23,38]. Following this, the radar image spectrum was obtained through a FFT and given as input to U-NET in order to reconstruct the wave spectrum and, consequently, estimate the sea state. A performance analysis of the proposed deep-learning estimation strategy is provided even through comparison with the classical MTF approach in [11].

The manuscript is organized as follows: Section 2 presents the numerical sea wave model and the approach for the radar image generation. The U-NET architecture is recalled in Section 3, and the numerical analysis is presented and discussed in Section 4. Conclusions follow in Section 5.

2. Synthetic Data

This section describes the models adopted for generating sea wave elevation and the corresponding raw radar image. Specifically, the JONSWAP spectrum [37] is assumed for the wave model, while for the radar image, a simplified geometrical approach, taking into account the tilt modulation, shadowing phenomenon [11], and the characteristics and operation conditions of a marine radar, is considered [23].

2.1. Numerical Sea Wave Model

The sea wave elevation is generated by employing the Fourier domain approach [34–36], already adopted in [7,8], under deep-sea water conditions [39]. According to [35], the wave elevation $\eta(\underline{r}, t)$ at time t and point $\underline{r} = (x, y)$ can be expressed as

$$\eta(\underline{r}, t) = \text{Re}\left\{ \int_{-\infty}^{\infty} \int_{-\infty}^{\infty} \widetilde{\eta}_0(\underline{k}) e^{-i(\underline{k} \cdot \underline{r} - \omega(\underline{k})t + \phi(\underline{k}))} dk_x dk_y \right\} \tag{1}$$

where $\underline{k} = (k_x, k_y)$ is the wave vector, $\widetilde{\eta}_0$ and ϕ are the amplitudes and random phase of each wave component identified by the wave vector $\underline{k}$, respectively, and Re{} is the real part operation.

According to the linear wave theory [39], ω is the angular frequency, which is related to $\underline{k}$ through the dispersion relation. In deep water conditions with no sea surface current, the latter is defined as $\omega(\underline{k}) = \sqrt{g|\underline{k}|}$, where g is the acceleration of gravity.

By employing the Fourier domain approach [34–36], the wave elevation in Equation (1) undergoes spatial sampling according to the discretization steps $(\Delta x, \Delta y)$. Similarly, the wave vector components are sampled with step $(\Delta k_x, \Delta k_y)$ determined by the discrete Fourier transform (DFT) theory. Therefore, we introduce the wave spectrum $E_w(\underline{k})$ obtained through FFT of the $\eta(\underline{r}, t)$ at a fixed time t. As we will see in Section 3.1, the amplitude of the wave spectrum $I_w(\underline{k}) = |E_w(\underline{k})|$ represents the U-NET ground truth image.

It should be noticed that, without the loss of generality, the analysis performed in this study does not account for the temporal sequence of the wave elevation but is based on a single-time snapshot of the wave field motion.

With regards to the spectral proprieties of the wave elevation, the 2D JONSWAP model $E_{JS}(\underline{k})$ is considered [37]. Therefore, the amplitudes of wave components are given by

$$\widetilde{\eta}_0(\underline{k}) = \sqrt{2E_{JS}(\underline{k})\Delta k_x \Delta k_y} \tag{2}$$

and the phase $\phi(\underline{k})$ is randomly generated from a uniform distribution between $[-\pi, \pi]$.

According to the assumed deep sea water model, the directional spectrum is expressed as follows:

$$E_{JS}(k, \theta) = \frac{0.0076}{2k^4} \left(\frac{U_{10}^2}{gL_f} \right)^{0.22} \exp\left[-1.25 \left(\frac{k_p}{k} \right)^2 \right] \gamma^{\varepsilon_k} \cdot D_{JS}(\theta) \tag{3}$$

$$\varepsilon_k = \exp\left[-\frac{1}{2\sigma^2} \left(\sqrt{\frac{k}{k_p}} - 1 \right)^2 \right] \tag{4}$$

$$\sigma = \begin{cases} 0.07, & |\underline{k}| \leq k_p \\ 0.06, & |\underline{k}| > k_p \end{cases} \tag{5}$$

where U_{10} is the wind speed at a height of 10 m above the mean sea level (MSL), L_f is the fetch length, k_p is the peak wave number, and σ is the peak shape parameter. Finally, $D_{JS}(\theta)$ is the directional spreading function defined in [40] as:

$$D_{JS}(\theta) = N_f \cos^{2s}(\theta - \theta_p) \tag{6}$$

where N_f and s are the normalization and spreading factors, respectively, θ is the propagation direction, and θ_p is the direction of the dominant wave (i.e., wind direction). The JONSWAP spectral parameters are summarized in Table 1 for convenience.

Table 1. JONSWAP spectral parameters.

Spectral Parameters	
L_f	Fetch length
U_{10}	Wind speed
k_p	Peak wave number
σ	Peak shape
N_f	Normalization factor
s	Spreading factor

Regarding the sea state parameters, the significant wave height H_s is the most common parameter to characterize the wave elevation field. This parameter can be derived from the wave spectrum defined in Equation (4) or, equivalently, by the variance ($var(\cdot)$) of wave elevation $\eta(\underline{r})$, i.e.,

$$H_s = 4\sqrt{\int_{-\infty}^{\infty}\int_{-\infty}^{\infty} E_{JS}(\underline{k})dk_y dk_x} = 4\sqrt{var(\eta(\underline{r}))} \tag{7}$$

On the other hand, the peak wavelength λ_p and the direction θ_p of the dominant wave can be estimated from the position of the peak of the wave spectrum amplitude $I_w(\underline{k})$.

2.2. Radar Image Simulation

Once the wave elevation $\eta(\underline{r})$ is generated via Equation (1), the corresponding radar image is produced by taking into account the main physical mechanisms responsible for the modulation of the radar signal [11], the characteristics and the operative conditions of a marine radar [23,38].

As shown in the 2D geometry of Figure 1, a radar mounted at a height h_r above the MSL illuminates, at ground range R, the scene with an incidence angle $\varphi = \tan^{-1}\left(\frac{R(\underline{r})}{h_r - \eta(\underline{r})}\right)$. In a typical configuration, the radar operates in near-grazing conditions, i.e., the incidence angle φ approaches $90°$.
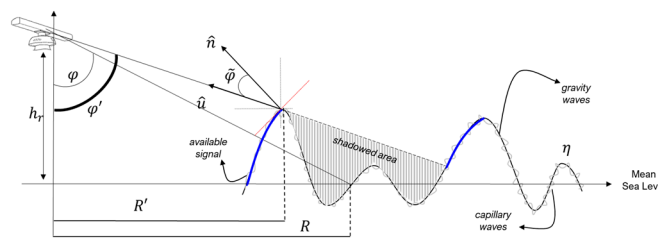
Figure 1. Graphical representation of the tilt modulation and shadowing phenomenon in the vertical plane. The blue curves indicate the illuminated parts of the sea surface.

The modulation of the radar signal amplitude (tilt modulation) depends on the local incidence angle $\widetilde{\varphi}$, defined by the incident ray $\hat{u}$, and the normal $\hat{n}$ to the wave surface [11,23], and it is given by

$$\xi(\underline{r}) = \hat{u}(\underline{r}) \cdot \hat{n}(\underline{r}) = \cos\widetilde{\varphi}(\underline{r}) \tag{8}$$

To a first approximation, the shadowing effect can be interpreted as a geometrical phenomenon occurring when the radar antenna does not receive any signal from the shadowed facet of the sea surface [11,23]. Therefore, the shadowing mask $m(\underline{r})$ is obtained when the following condition holds:

$$\exists\,(R, \varphi): \varphi < \varphi',\ R\prime < R \tag{9}$$

Moreover, the sea surface can be seen as a superposition of long (gravity) waves and short (capillary) waves. The small ripples are responsible for the main backscattering contribution (resonant Bragg scattering), which is modulated by longer waves detected by the radar. According to [23], the received signal power is proportional to the normalized radar cross section (NRCS) of the sea surface, which is in turn proportional to $\cos^4 \widetilde{\varphi}(\underline{r})$. Furthermore, by accounting for shadowing and the presence of a uniformly distributed multiplicative speckle noise $q(\underline{r})$, the NRCS can be written as

$$\eta_{NRCS}(\underline{r}) = \left(\cos \widetilde{\varphi}(\underline{r})\right)^4 \cdot m(\underline{r}) \cdot q(\underline{r}) \tag{10}$$

Since the radar image is a measure of the received signal power at the output of the radar amplifier, the radar equation ([23,38]) is applied in the logarithmic form to get the radar amplifier response (RAR):

$$\eta_{RAR}(\underline{r}) = \log[\eta_{NRCS}(\underline{r})] - 3\log(R) \tag{11}$$

The RAR defined by Equation (11) undergoes a digitalization process, which in this study is supposed to be a 16-bit quantization, thereby getting the radar image:

$$\eta_{radar}(\underline{r}) = \text{digitalization}\{\log[\eta_{RAR}(\underline{r})]\} \tag{12}$$

At this point, it is possible to introduce the radar spectrum $E_r(\underline{k})$ obtained through a double FFT of the $\eta_{radar}(\underline{r})$. As shown in Section 3.1, the amplitude of the radar spectrum $I_r(\underline{k}) = |E_r(\underline{k})|$ represents the input image of U-NET.

3. Directional Spectrum and Wave Elevation Reconstruction

This section describes the U-NET architecture, the dataset generated to train the network, and presents the metrics used to assess the reliability of the obtained results. Additionally, the metrics for the assessment of the wave elevation reconstruction and derived significant wave height are provided.

3.1. Deep Learning-Based Strategy

3.1.1. U-Net Architecture

U-NET [30] has a symmetric encoder–decoder structure whose input and output are the amplitude of the radar spectrum $I_r(\underline{k})$ and wave spectrum $I_w(\underline{k})$, respectively. As the name suggests, the network is characterized by a U-shape (see Figure 2) where the left part (encoder) extracts features from the input radar image spectrum $I_r(\underline{k})$ by means of convolutional and pooling layers that progressively decrease the data size and increase the number of feature maps. On the other hand, the right part of the network (decoder) provides the wave spectrum $I_w(\underline{k})$ through upsampling and convolutional layers that progressively increase the spatial resolution of the encoded features and reduce the number of feature maps. It should be noted that the amplitudes of the radar image spectrum and that of the wave field spectrum are not directly comparable. Therefore, to simplify the training process, the amplitude of the images is rescaled to vary in the interval [0, 1]. The network consists of three levels. The input image $I_r(\underline{k})$ has dimensions 256 × 128 and is processed by a sequence of three 3 × 3 convolutions, each one followed by a batch normalization (BN) and rectified linear unit (ReLu) activation function. The convolutional layers extract multiple feature maps, with the number of maps increasing in the lower levels, while the image dimensions remain unchanged after each convolution due to the use of zero padding. A 2 × 2 max pooling operation (indicated by violet arrows) halves the dimensions of the feature maps as they move from one level to the next. In the second and third levels, two convolutions per level are performed, with each convolution followed by BN and ReLU. At the third level, the feature maps have dimensions of 64 × 32.
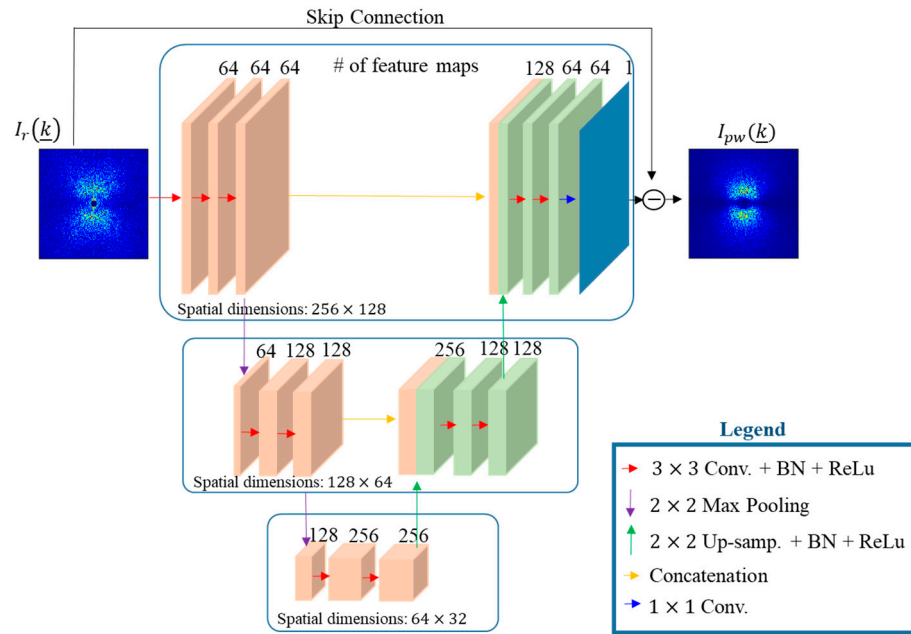
Figure 2. Representation of U-NET architecture.

The network's ascending path begins with a 2×2 upsampling that doubles the dimensions of each feature map, followed by BN and a ReLU activation (indicated by the green arrow). Next, half of these feature maps are merged (yellow arrow) with the corresponding cropped feature maps from the descending path. Afterwards, two 3×3 convolutions are performed, along with BN and ReLU. This process continues until it reaches the first level of the network, where a 1×1 convolution reduces the feature maps to form a single image. This image is then subtracted from the input image via a skip connection, facilitating residual learning to counteract the vanishing gradient problem [41].

The U-NET output image is the predicted amplitude of the wave spectrum $I_{pw}(\underline{k})$, which is used for the wave field reconstruction. The squared error averaged over the mini-batch is considered as loss function for network training [33].

The sea wave field reconstruction is performed by applying the double IFFT to the wave amplitude spectrum and the phase spectrum as follows:

$$\eta_{UNet}(\underline{r}) = Re\left\{ \int_{-\infty}^{\infty} \int_{-\infty}^{\infty} I_{pw}(\underline{k}) e^{-i(\underline{k}\cdot\underline{r} - \phi_r(\underline{k}))} dk_x dk_y \right\} \qquad (13)$$

As regards the phase of the wave spectrum, this quantity is retrieved from the phase of the radar spectrum $\phi_r(\underline{k}) = tan^{-1}\left(\frac{\Im m\{E_r(\underline{k})\}}{Re\{E_r(\underline{k})\}} \right)$ by subtracting a constant phase shift equal to $sign\{|\underline{k}|\}\cdot\pi/2$ [42–44]. Here, $\Im m\{\}$ and $sign\{\}$ denote the imaginary part operation and the signum function, respectively.

3.1.2. Dataset Generation

The synthetic wave elevation dataset considered for the training, validation, and testing of U-NET is generated according to the numerical model detailed in Section 2.1. Specifically, $N_r = 30,000$ realizations are generated with the JONSWAP parameters L_f, U_{10}, γ, and s randomly taken from a uniform distribution within the given ranges specified in Table 2. Given the JONSWAP parameters, the sea state parameters H_s, λ_p, and T_p are derived, and their ranges are indicated in Table 2, while their distributions are depicted in Figure 3. For each combination of sea state parameters, the dominant wave direction θ_p is randomly assigned from a uniform distribution over the discrete set of values $[0, 20, 45, 300, 330]°$. It should be noticed that the random phase $\phi(\underline{k})$ involved in the generation of the sea wave elevation (see Equation (1)) varies for each sample in the dataset.

Table 2. Variation ranges of JONSWAP and derived sea state parameters.

	JONSWAP Parameters				Sea State Parameters		
	L_f [km]	U_{10} [m/s]	γ	s	H_s [m]	λ_p [m]	T_p [s]
Minimum value	50	5	1	1	0.69	23	3.4
Maximum value	350	15	7	4	6.67	169.4	10.48
Step	-	-	1	1	-	-	-
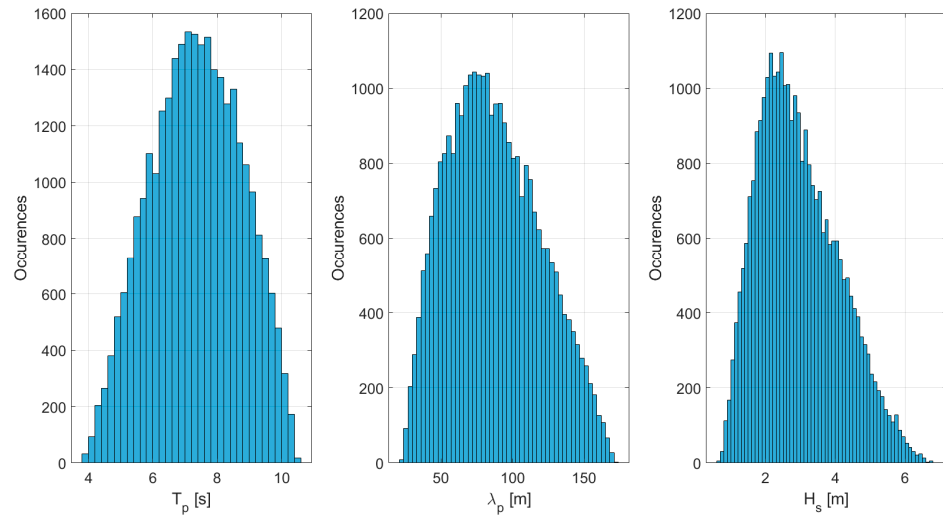
Figure 3. Distribution of the sea state parameters.

The wave elevation field $\eta(\underline{r})$ is evaluated over a Cartesian grid with size 256×128 and a spatial discretization step $\Delta x = \Delta y = 7.5$ m. The corresponding radar image is simulated by considering the radar antenna to be fixed at a height $h_r = 30$ m above MSL and located at coordinates $(0,0)$ m. Additionally, a radar blind zone with a radius equal to 150 m is set, and a multiplicative speckle noise $q(\underline{r})$ uniformly distributed with a zero mean and variance equal to 0.1 is considered for the radar image.

Figure 4 shows an example of the wave elevation field and the corresponding radar image, as well as the amplitude of the directional wave spectrum and radar image spectra. It can be seen that the radar image spectrum has similar spatial information compared to the wave spectrum. However, the radar image spectrum exhibits several distortions due to radar imaging mechanisms (e.g., tilt modulation and shadowing) that need to be corrected.

The dataset is divided as follows: N_{tr} =21,000 samples are assigned for training, N_{val} =3000 samples are reserved for validation, and the remaining N_{test} =6000 samples are designated for testing.

3.1.3. Network Testing Performance Metrics

The effectiveness of the proposed strategy is evaluated by comparing the predicted amplitude of the wave spectrum $I_{pw}(\underline{k})$ with the ground truth $I_w(\underline{k})$. Specifically, this comparison is quantified for each sample in the test dataset in terms of the root mean square error (*RMSE*)

$$RMSE = \sqrt{\frac{1}{Q}\sum_{i=1}^{Q}\left|I_{w_i} - I_{pw_i}\right|^2}, \tag{14}$$

and the mean percentage error (*MPE*)

$$MPE = \frac{\sum_{i=1}^{Q}\left|I_{w_i} - I_{pw_i}\right|^2}{\sum_{i=1}^{Q}\left|I_{w_i}\right|^2} \times 100, \tag{15}$$

where $Q = 256 \times 128$ is the number of pixels in the images $I_w(\underline{k})$ and $I_{pw}(\underline{k})$, respectively.
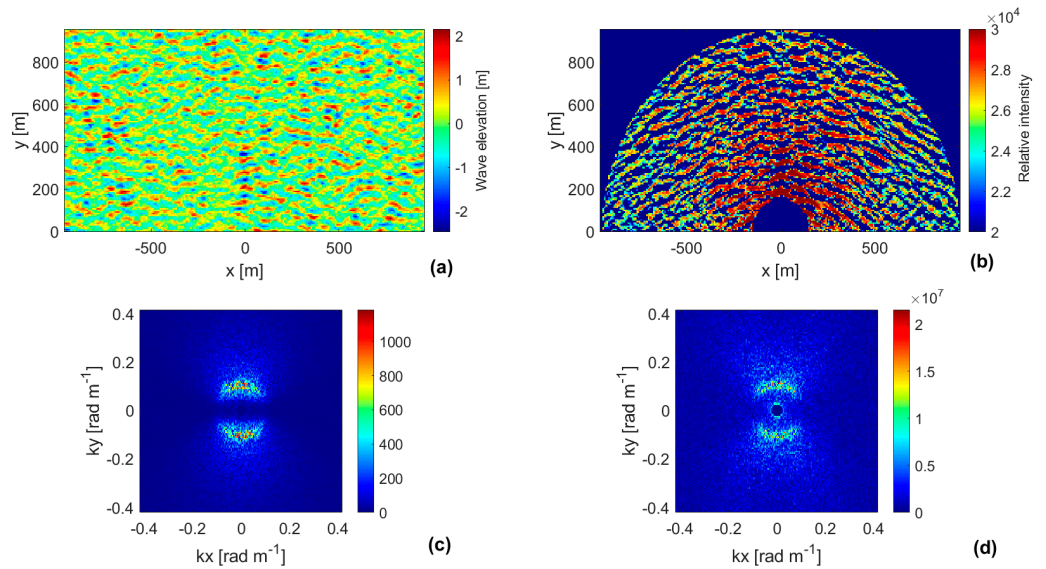
Figure 4. (**a**) Simulated wave field; (**b**) simulated radar image; (**c**) directional wave spectrum; (**d**) directional radar image spectrum.

3.2. Metrics for Wave Reconstruction

The similarity between the ground truth $\eta(\underline{r})$ and the reconstructed wave elevation fields $\eta_{rec}(\underline{r})$ ($\eta_{MTF}(\underline{r})$ or $\eta_{UNET}(\underline{r})$), is assessed using the linear correlation coefficient (CC) and the relative percentage error (*RPE*) normalized to H_s [45]. Their definitions are given by

$$CC = \frac{\sum_{\underline{r}} \left(\eta(\underline{r}) - \widetilde{\eta} \right) \left(\eta_{rec}(\underline{r}) - \widetilde{\eta}_{rec} \right)}{\sqrt{\sum_{\underline{r}} \left(\eta(\underline{r}) - \widetilde{\eta} \right)^2 \left(\eta_{rec}(\underline{r}) - \widetilde{\eta}_{rec} \right)^2}} \tag{16}$$

and

$$RPE = \frac{|\eta(\underline{r}) - \eta_{rec}(\underline{r})|}{H_s} \times 100 \tag{17}$$

where $\widetilde{\eta}$ and $\widetilde{\eta}_{rec}$ represent the corresponding average values of the ground truth and the reconstructed wave elevation fields, respectively. Furthermore, the details regarding the reconstruction of the wave elevation field using the MTF approach are reported in Appendix A.

On the other hand, the accuracy of the retrieved significant wave height is quantified by considering the metrics *CC*, *RMSE*, and *MPE* and defined as

$$CC = \frac{\sum_{i=1}^{N_{test}} \left(H_{si} - \widetilde{H}_s \right) \left(H_{s_{est_i}} - \widetilde{H}_{s_{est}} \right)}{\sqrt{\sum_{i=1}^{N_{test}} \left(H_{si} - \widetilde{H}_s \right)^2 \left(H_{s_{est_i}} - \widetilde{H}_{s_{est}} \right)^2}} \tag{18}$$

$$RMSE = \sqrt{\frac{1}{N_{test}} \sum_{i=1}^{N_{test}} \left| H_{si} - H_{s_{est_i}} \right|^2} \tag{19}$$

$$MPE = \frac{\sum_{i=1}^{N_{test}} |H_{s_i} - H_{s_{est_i}}|^2}{\sum_{i=1}^{N_{test}} |H_{s_i}|^2} \times 100 \tag{20}$$

Depending on the adopted strategy, the quantity H_{sest} in Equations (19) and (20) may refer to $H_{s_{UNet}}$ or $H_{s_{MTF}}$ (see Appendix A). In the same way, $\widetilde{H}_s$ and $\widetilde{H}_{s_{est}}$ denote the average values of the true and estimated significant wave height, respectively.

4. Numerical Results

This section describes the results of the numerical simulations achieved by applying the deep learning strategy outlined in Section 3.
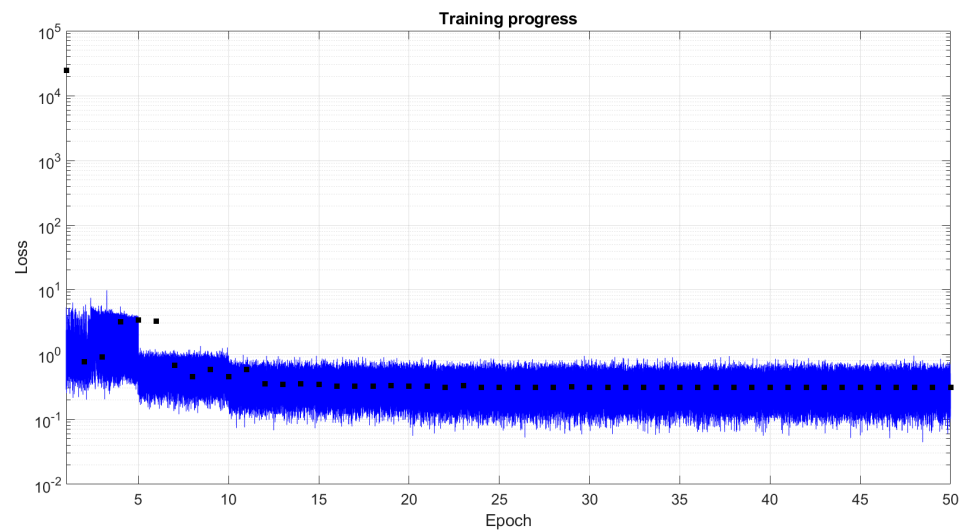
4.1. Network Training

The network is trained by considering the training options and the hyperparameters' settings summarized in Table 3. A grid search involving some key hyperparameters is performed to ensure good network training. As seen in Table 3, three different values of mini-batch size and initial learning rates are considered together with the ADAptive Moment estimation (ADAM) optimizer. The adaptive learning rate halves every 5 epochs up to a maximum number of 50 epochs.

Table 3. U-NET training settings.

Option/Parameter	Description/Value
Mini-batch size	$(2, 4, 8)$
Initial learning rate	$(10^{-3}, 10^{-2}, 10^{-1})$
Optimizer	ADAM
Learning rate drop period	5
Learning rate drop factor	0.5
Gradient threshold method	'absolute value'
Gradient threshold	0.01
Shuffle	'every epoch'
Max. number of epochs	50

The network training is performed via MATLAB 2023a Deep Learning Toolbox (Mathworks, Natick, MA, USA) on a NVIDIA (Santa Clara, CA, USA) Quadro GPU equipped with 2304 CUDA® cores and 8 GB GDDR6 RAM. The total computation time is about 68 h, and the best results are obtained for mini-batch size and the initial learning rate equal to 4 and 10^{-3}, respectively.

Figure 5 shows the training and validation versus the number of epochs. It can be seen that the curves are in agreement, and the loss values converge after about 12 epochs.

Figure 5. Training (blue line) and validation (black squares) loss versus number of epochs.

Figure 6 illustrates the network operation on five samples randomly selected from the test dataset. The first, second, and third rows represent the input $I_r(\underline{k})$, output $I_{pw}(\underline{k})$, and ground truth $I_w(\underline{k})$ images, respectively. The input images are filtered employing a high-pass filter with a cutoff wavelength $\lambda_{cutoff} = 190$ m, to remove the strong noise contribution introduced at low wavenumbers by the modulation phenomena and range

dependency. Despite that, as can be observed, the network predictions highlight a good agreement with the corresponding ground truth images. Notably, the spreading of the wave spectrum energy towards the high wavenumbers observed in the input images is quite well compensated.
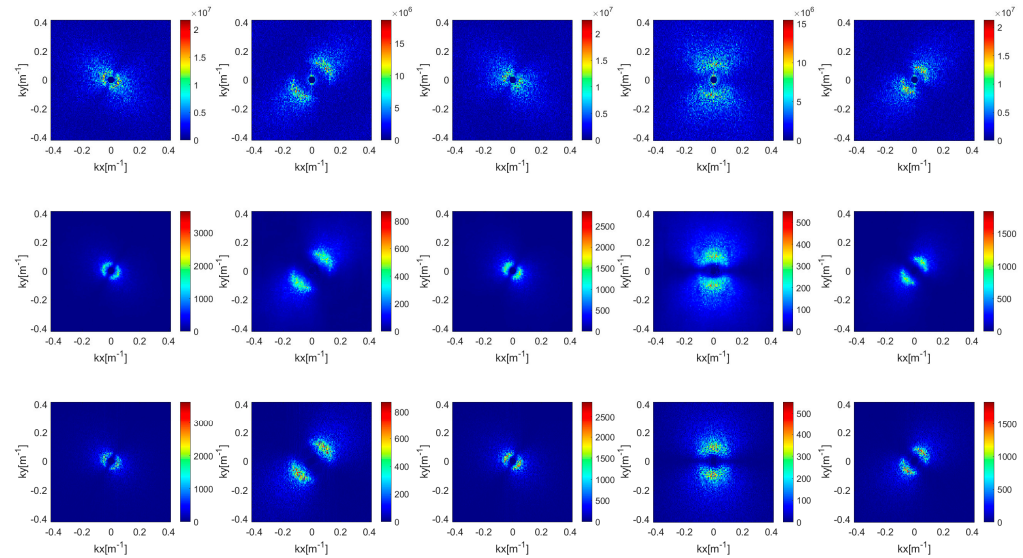

Figure 6. Five samples randomly chosen in the test dataset. Input (first row). Output (second row). Ground truth (third row).

A quantitative assessment of network performance is carried out in terms of the *MPE* and RMSE for each sample in the test dataset (see Figure 7). Specifically, the mean error values (e.g., *MPE* = 15.7% and *RMSE* = 0.0042) indicate that the network predictions effectively compensate for the distortions introduced by the radar sensing process and quite accurately recover the spectrum amplitude.

4.2. Retrieval of Wave Elevation and Wave Parameters

The wave elevation field is determined using the wave spectrum amplitude predicted by U-NET and applying Equation (13). In detail, for each sample in the test dataset, the retrieved wave elevation is compared to the ground truth. Additionally, a comparison with the reconstruction obtained by applying the MTF is also included (see Equation (A3) in Appendix A). The quantitative performance analysis is provided through the *CC* and *RPE* metrics introduced in Section 3.2, whose average values are listed in Table 4. Moreover, an example of the wave elevation field $\eta(\underline{r})$, with sea state parameters $\lambda_p = 118$ m, $\theta_p = 0°$, $H_s = 4.62$ m, and its reconstruction $\eta_{MTF}(\underline{r})$ and $\eta_{UNET}(\underline{r})$, is reported in Figure 8, while the *RPE* maps are displayed in Figure 9. Concerning the average *CC* and *RPE*, it is evident that both strategies exhibit limited accuracy in wave elevation reconstruction. This outcome is primarily attributed to the use of radar phase for wave reconstruction (see Equations (13) and (A3)). However, it is well established that in this context, a better performance in wave field reconstruction and sea state parameters' estimation are achieved by considering an angular sector around the direction of the incoming sea wave [7]. Hence, to enhance the reconstruction accuracy, an angular sector of ±35° around the incoming wave direction is selected (indicated by the red lines in Figure 9), resulting in significantly improved average *CC* and *RPE* (refer to Table 4).
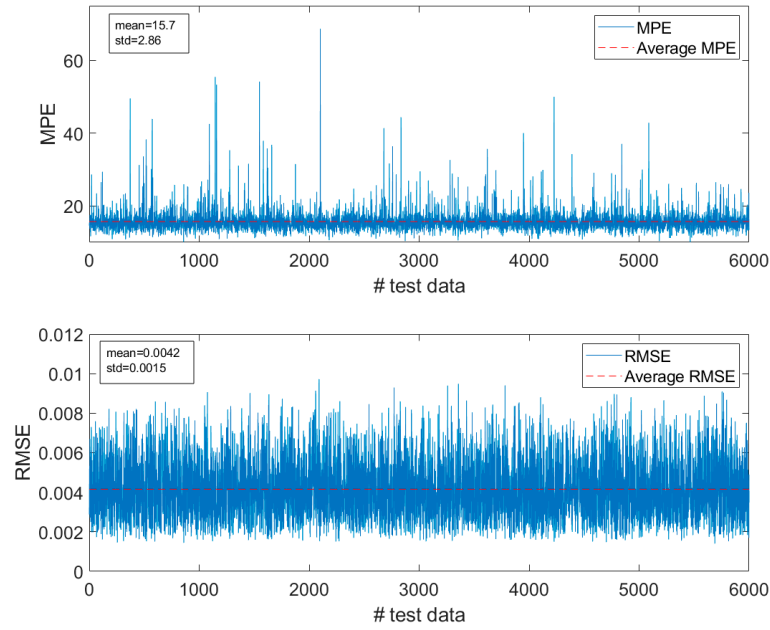
Figure 7. The curves of *MPE* and *RMSE* for each sample in the test dataset. The red dashed lines denote the average values of the former quantities.

Table 4. Performance analysis of the wave elevation reconstruction.

Metrics	η_{UNet}	η_{MTF}
CC	0.56	0.50
$CC_{\pm 35°}$	0.81	0.76
RPE	16%	18%
$RPE_{\pm 35°}$	11%	14%
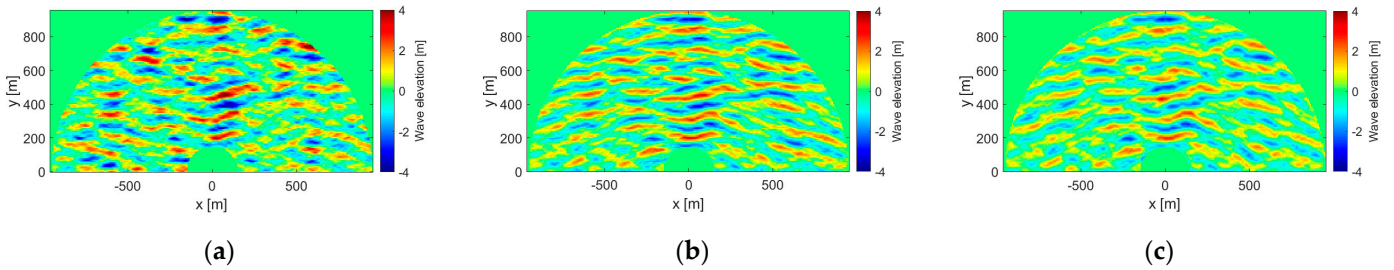
Figure 8. Wave elevation field (**a**) ground truth; (**b**) reconstructed by U-NET strategy; (**c**) reconstructed by MTF strategy.
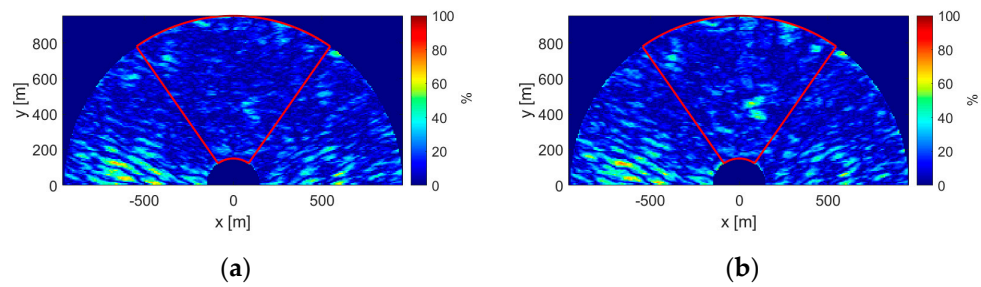
Figure 9. Relative percentage error (**a**) U-NET; (**b**) MTF. The red lines indicate an angular sector of $\pm 35°$ around the incoming wave direction.

The significant wave height is estimated within the reliable angular sector, and the performance of the U-NET and MTF strategies is compared in Table 5 and Figure 10. As observed, the U-NET strategy notably outperforms MTF in estimating H_s from the reconstructed wave field. Figure 10 clearly shows that the MTF approach tends to overestimate and underestimate the low and high H_s values, respectively. This occurs because MTF is an empirical function that needs to be adapted for each sea state [18,44]. Note that the calibration coefficient c defined in Equation (A4) (refer to Appendix A) is taken as the average of the coefficients calculated across all the considered training dataset. Additionally, a fixed coefficient β has been used for all testing samples (see Appendix A), which can amplify artifacts at low wavenumbers in the radar image spectrum, especially for wave fields characterized by small wavelengths. This phenomenon leads to incorrect wave field reconstruction and consequently inaccurate sea state parameters' estimation.

Table 5. Performance analysis of the H_s estimation.

Metrics	$H_{s\,UNet}$	$H_{s\,MTF}$
CC	0.97	0.95
MPE	0.79%	2.82%
RMSE	0.28 [m]	0.53 [m]
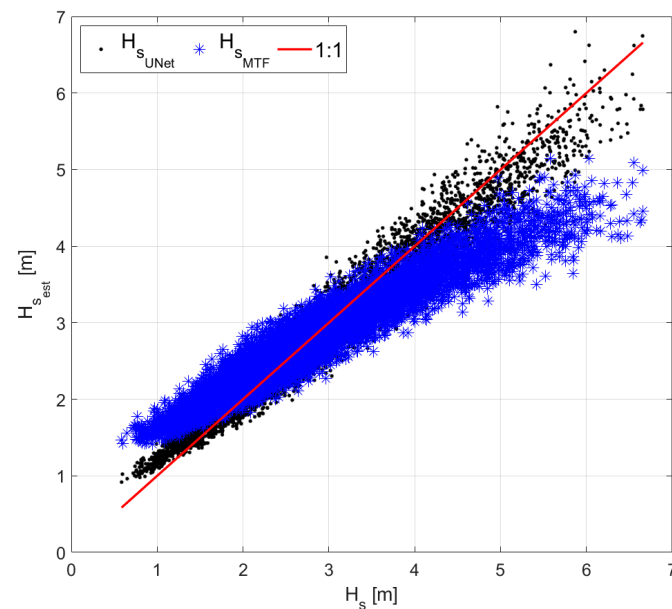
Figure 10. Scatter plots between ground truth H_s versus estimated H_s.

Finally, Figure 11 shows three wave elevation profiles with incoming waves at $\theta_p = 0°$ and varying λ_p and H_s values. It is evident that the reconstruction achieved using the U-NET strategy outperforms the MTF method. Additionally, for small wavelengths (see Figure 11a), the reconstruction η_{MTF} is very inaccurate.
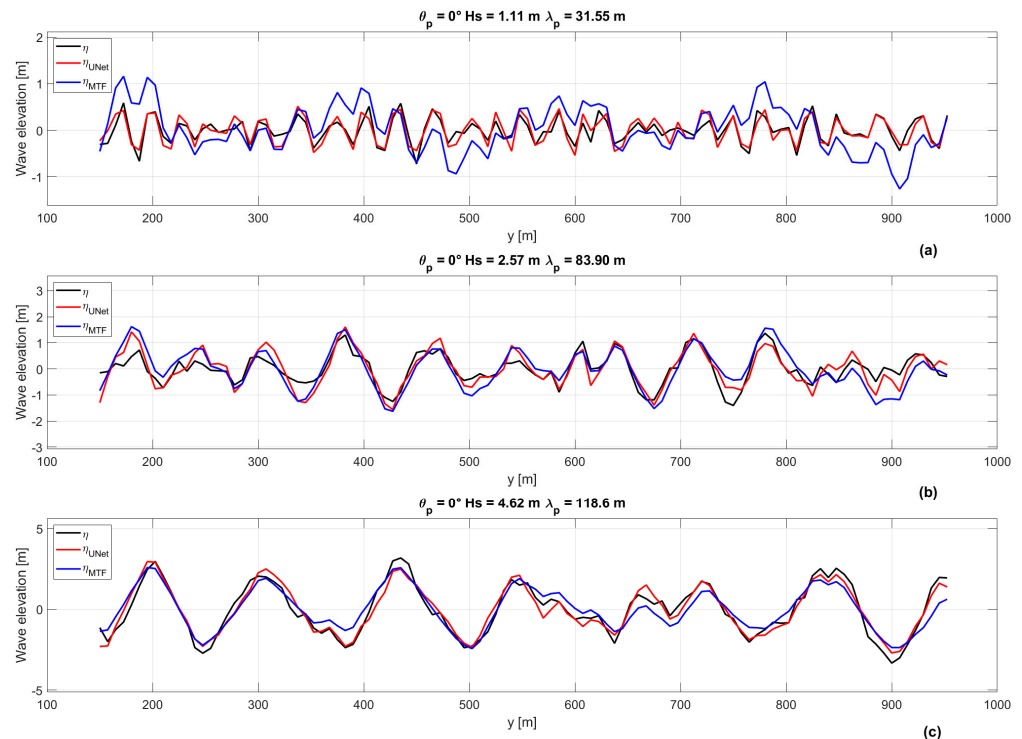
Figure 11. Examples of the reconstructed wave elevation profiles. (**a**) $H_s = 1.11$ [m]; (**b**) $H_s = 2.57$ [m]; (**c**) $H_s = 4.62$ [m].

5. Conclusions

This manuscript has proposed a deep learning approach based on U-NET for reconstructing the sea wave spectrum from the marine radar data. A synthetic dataset of wave elevation field with significant wave height values ranging from 0.69 m to 6.67 m has been generated considering the spectral proprieties of the JONSWAP model. For each wave field realization, the radar imaging mechanisms (tilt and shadowing modulation) have been applied to generate the radar image spectrum. This radar image spectrum has been considered as the input of the network, which provides an estimate of the sea wave spectrum as its output. A performance analysis in terms of *MPE* and *RMSE* has demonstrated that the proposed approach is effective for different sea wave conditions. The wave spectra retrieved via U-NET have allowed reconstructing the wave elevation field and estimating the significant wave height. Numerical results have confirmed that the proposed approach is more accurate than the classical MTF strategy, both in reconstructing wave elevation fields, especially in the direction of the incoming waves, and in retrieving sea state parameters.

Future research activities will focus on the experimental validation of the proposed technique.

Author Contributions: Conceptualization, G.L. and G.G.; methodology, G.L. and G.G.; software, G.L., G.E. and G.G.; validation, G.L., G.E. and G.G.; formal analysis, G.L., G.E. and G.G.; investigation, G.L., G.E. and G.G.; resources, G.L., G.E. and G.G.; data curation, G.L., G.E. and G.G.; writing—original draft preparation, G.L., G.E. and G.G.; writing—review and editing, G.L., G.G. and G.E.; supervision, F.S. and C.L.; project administration, G.L. and C.L.; funding acquisition, G.L., C.L. and F.S. All authors have read and agreed to the published version of the manuscript.

Appendix A

MTF-Based Strategy

The MTF strategy is partly linked to the linear interpretation of tilt modulation, as discussed in [44,46]. However, because of the nonlinearities caused by the shadowing effect and, to a lesser degree, by tilt modulation, the derivation of the MTF typically relies on a posteriori fitting procedure such as the ones mentioned in [11,16,17]. Therefore, due to nonlinearities, the MTF should be tuned to the specific sea state and the specific sea environments, as proposed in [47] for coastal areas. In the general form, the MTF is calculated as the ratio between the amplitudes of the radar signal spectrum and the wave elevation spectrum as a function of the wave number, i.e.,

$$\mathcal{M}(\underline{k}) = \frac{I_r(\underline{k})}{I_w(\underline{k})} \tag{A1}$$

However, in this study, the MTF strategy proposed in [11] is adopted since it represents a standard approach for obtaining wave spectra from radar spectra. Specifically, the MTF is defined as $\mathcal{M}(\underline{k}) = |\underline{k}|^\beta$, where β is an empirical coefficient set at 1.2, according to [11]. Starting from the amplitude $I_r(\underline{k})$ of the radar image spectrum, the reconstructed amplitude is calculated as:

$$I_{MTF}(\underline{k}) = I_r(\underline{k})/\mathcal{M}(\underline{k}) \tag{A2}$$

To this end, as in Equation (7), the wave elevation reconstruction is achieved by applying the double IFFT to the $I_{MTF}(\underline{k})$ and shifted phase spectrum $\phi_r(\underline{k})$, i.e.,

$$\eta_{MTF}(\underline{r}) = \text{Re}\left\{ \int_{-\infty}^{\infty}\int_{-\infty}^{\infty} I_{MTF}(\underline{k}) e^{-i(\underline{k}\cdot\underline{r}-\phi_r(\underline{k}))} dk_x dk_y \right\} \tag{A3}$$

The MTF provided an unscaled wave spectrum amplitude and, hence, an unscaled wave elevation reconstruction. Therefore, a calibration coefficient is defined using the relationship between the variance of wave elevation $\eta_{MTF}(\underline{r})$ and the ground truth of the significant wave height H_s, given by

$$c = \frac{H_s}{4\sqrt{var(\eta_{MTF}(\underline{r}))}} \tag{A4}$$

and the $H_{s\,MTF} = 4c\cdot\sqrt{var(\eta_{MTF})}$.

References

1. Shearman, E.D.R. Radio science and oceanography. *Radio Sci.* **1983**, *18*, 299–320. [CrossRef]
2. Ludeno, G.; Uttieri, M. Editorial for Special Issue "Radar Technology for Coastal Areas and Open Sea Monitoring". *J. Mar. Sci. Eng.* **2020**, *8*, 560. [CrossRef]
3. Roarty, H.; Cook, T.; Hazard, L.; George, D. The Global High Frequency Radar Network. *Front. Mar. Sci.* **2019**, *6*, 164. [CrossRef]
4. Maa, J.P.-Y. X-band radar wave observation system. In *Field Testing of a Physical/Biological Monitoring Methodology for Offshore Dredging and Mining Operations*; U.S. Department of the Interior, Minerals Management Service: Herndon, VA, USA, 2006; 84p.

5. Ardhuin, F.; Aksenov, Y.; Benetazzo, A.; Bertino, L.; Brandt, P.; Caubet, E.; Chapron, B.; Collard, F.; Cravatte, S.; Delouis, J.-M.; et al. Measuring currents, ice drift, and waves from space: The Sea Surface Kinematics Multiscale monitoring (SKIM) concept. *Ocean Sci.* **2018**, *14*, 337–354. [CrossRef]

6. Natale, A.; Jackson, G.; Esposito, C.; Fornaro, G.; Lanari, R.; Perna, S. Sea state observation through a three-antenna hybrid XT/AT InSAR configuration: A preliminary study based on the InSAeS4 airborne system. *Remote Sens.* **2017**, *9*, 792. [CrossRef]

7. Ludeno, G.; Catapano, I.; Soldovieri, F.; Gennarelli, G. Retrieval of Sea Surface Currents and Directional Wave Spectra by 24 GHz FMCW MIMO Radar. *IEEE Trans. Geosci. Remote Sens.* **2023**, *61*, 1–13. [CrossRef]

8. Ludeno, G.; Antuono, M.; Soldovieri, F.; Gennarelli, G. A Feasibility Study of Nearshore Bathymetry Estimation via Short-Range K-Band MIMO Radar. *Remote Sens.* **2024**, *16*, 261. [CrossRef]

9. Cui, J.; Bachmayer, R.; de Young, B.; Huang, W. Experimental Investigation of Ocean Wave Measurement Using Short-Range K-Band Radar: Dock-Based and Boat-Based Wind Wave Measurements. *Remote Sens.* **2019**, *11*, 1607. [CrossRef]

10. Carrasco, R.; Nieto-Borge, J.-C.; Seemann, J.; Horstmann, J. Significant Wave Height Retrieved From Coherent X-Band Radar: A Physics-Based Approach. *IEEE Trans. Geosci. Remote Sens.* **2024**, *62*, 1–15. [CrossRef]

11. Borge, J.C.N.; Rodriguez, G.R.; Hessner, K.; González, P.I. Inversion of marine radar images for surface wave analysis. *J. Atmos. Ocean. Technol.* **2004**, *21*, 1291–1300. [CrossRef]

12. Wei, Y.; Zheng, Y.; Lu, Z. A Method for Retrieving Wave Parameters From Synthetic X-Band Marine Radar Images. *IEEE Access* **2020**, *8*, 204880–204890. [CrossRef]

13. Plant, W.J.; Keller, W.C. Evidence of Bragg scattering in microwave Doppler spectra of seareturn. *J. Geophys. Res.* **1990**, *95*, 16299–16310. [CrossRef]

14. Lee, P.H.Y.; Barter, J.D.; Beach, K.L.; Hindman, C.L.; Lade, B.M.; Rungaldier, H.; Shelton, J.C.; Williams, A.B.; Yee, R.; Yuen, H.C. X-Band Microwave Backscattering from Ocean Waves. *J. Geophys. Res.* **1995**, *100*, 2591–2611. [CrossRef]

15. Wenzel, L.B. Electromagnetic scattering from the sea at low grazing angles. In *Suface Waves and Fluxes*; Geernaert, G.L., Plant, W.J., Eds.; Kluwer Academic: Norwell, MA, USA, 1990; pp. 41–108.

16. Chen, Z.; Zhang, B.; He, Y.; Qiu, Z.; Perrie, W. A new modulation transfer function for ocean wave spectra retrieval from X-band marine radar imagery. *Chin. J. Oceanol. Limnol.* **2015**, *33*, 1132–1141. [CrossRef]

17. Qiu, J.; Zhang, B.; Chen, Z.; He, Y. A New Modulation Transfer Function With Range and Azimuth Dependence for Ocean Wave Spectra Retrieval From X-Band Marine Radar Observations. *IEEE Geosci. Remote Sens. Lett.* **2017**, *14*, 1373–1377. [CrossRef]

18. Støle-Hentschel, S.; Carrasco, R.; Nieto-Borge, J.C.; Seemann, J.; Toledo, Y. Improved estimation of the directional wave spectrum from marine radar images by employing a directional modulation transfer function (MTF). *ESS Open Arch.* **2024**. [CrossRef]

19. Wijaya, A.P.; van Groesen, E. Determination of the significant wave height from shadowing in synthetic radar images. *Ocean Eng.* **2016**, *114*, 204–215. [CrossRef]

20. Gangeskar, R. An Algorithm for Estimation of Wave Height From Shadowing in X-Band Radar Sea Surface Images. *IEEE Trans. Geosci. Remote Sens.* **2014**, *52*, 3373–3381. [CrossRef]

21. Wei, Y.; Song, H.; Lei, Y.; Liu, K.; Lu, Z. A method of retrieving significant wave height based on shadowing from X-band marine radar images. *Int. J. Remote Sens.* **2023**, *44*, 5259–5282. [CrossRef]

22. Ludeno, G.; Serafino, F. Estimation of the Significant Wave Height from Marine Radar Images without External Reference. *J. Mar. Sci. Eng.* **2019**, *7*, 432. [CrossRef]

23. Salcedo-Sanz, S.; Borge, J.C.N.; Carro-Calvo, L.; Cuadra, L.; Hessner, K.; Alexandre, E. Significant wave height estimation using SVR algorithms and shadowing information from simulated and real measured X-band radar images of the sea surface. *Ocean Eng.* **2015**, *101*, 244–253. [CrossRef]

24. Cornejo-Bueno, L.; Borge, J.N.; Alexandre, E.; Hessner, K.; Salcedo-Sanz, S. Accurate estimation of significant wave height with Support Vector Regression algorithms and marine radar images. *Coast. Eng.* **2016**, *114*, 233–243. [CrossRef]

25. Park, J.; Ahn, K.; Oh, C.; Chang, Y.S. Estimation of Significant Wave Heights from X-Band Radar Using Artificial Neural Network. *J. Korean Soc. Coast. Ocean Eng.* **2020**, *32*, 561–568. [CrossRef]

26. Duan, W.; Yang, K.; Huang, L.; Ma, X. Numerical Investigations on Wave Remote Sensing from Synthetic X-Band Radar Sea Clutter Images by Using Deep Convolutional Neural Networks. *Remote Sens.* **2020**, *12*, 1117. [CrossRef]

27. Huang, W.M.; Yang, Z.D.; Chen, X.W. Wave Height Estimation From X-Band Nautical Radar Images Using Temporal Convolutional Network. *IEEE J. Stars* **2021**, *14*, 11395–11405. [CrossRef]

28. Kwon, J.W.; Chang, W.D.; Yang, Y.J. Significant wave height prediction from X-band marine radar images using deep learning with 3D convolutions. *PLoS ONE* **2023**, *18*, e0292884. [CrossRef]

29. Zhao, M.; Zheng, Y.; Lin, Z. Sea surface reconstruction from marine radar images using deep convolutional neural networks. *J. Ocean Eng. Sci.* **2023**, *8*, 647–661. [CrossRef]

30. Ronneberger, O.; Fischer, P.; Brox, T. U-net: Convolutional networks for biomedical image segmentation. In *Medical Image Computing and Computer-Assisted Intervention–MICCAI 2015: 18th International Conference, Munich, Germany, October 5–9, 2015, Proceedings, Part III*; Springer: Cham, Switzerland, 2015.

31. Jin, K.H.; McCann, M.T.; Froustey, E.; Unser, M. Deep convolutional neural network for inverse problems in imaging. *IEEE Trans. Image Proc.* **2017**, *26*, 4509–4522. [CrossRef]

32. Capozzoli, A.; Catapano, I.; Curcio, C.; D'Ambrosio, G.; Esposito, G.; Gennarelli, G.; Liseno, A.; Ludeno, G.; Soldovieri, F. Resolution-Enhanced Electromagnetic Inverse Source: A Deep Learning Approach. *IEEE Antennas Wirel. Propag. Lett.* **2023**, *22*, 2812–2816. [CrossRef]

33. Esposito, G.; Catapano, I.; Ludeno, G.; Soldovieri, F.; Gennarelli, G. A Deep Learning Strategy for Multipath Ghosts Filtering via Microwave Tomography. *IEEE Trans. Geosci. Remote Sens.* **2023**, *62*, 1–14. [CrossRef]

34. Mastin, G.; Watterberg, P.; Mareda, J. Fourier Synthesis of Ocean Scenes. *Comput. Graph. Appl.* **1987**, *7*, 16–23. [CrossRef]

35. Tessendorf, J. Simulating Ocean Water. SIG-GRAPH'99 Course Note. 2001. Available online: https://www.researchgate.net/publication/264839743_Simulating_Ocean_Water (accessed on 4 September 2024).

36. Fréchot, J. Realistic simulation of ocean surface using wave spectra. In Proceedings of the First International Conference on Computer Graphics Theory and Applications (GRAPP 2006), Setúbal, Portugal, 25–28 February 2006; pp. 76–83.

37. Hasselmann, K.; Barnett, T.P.; Bouws, E.; Carlson, H.; Cartwright, D.E.; Enke, K.; Ewing, J.A.; Gienapp, A.; Hasselmann, D.E.; Kruseman, P.; et al. Measurements of wind-wave growth and swell decay during the Joint North Sea Wave Project (JONSWAP). *Ergaenzungsheft Dtsch. Hydrogr. Z. Reihe A* **1973**. Available online: https://pure.mpg.de/rest/items/item_3262854_4/component/file_3282032/content (accessed on 4 September 2024).

38. Skolnik, M.I. *Introduction to Radar Systems*; McGraw-Hill Higher Education: New York, NY, USA, 2002.

39. Holthuijsen, L.H. *Waves in Oceanic and Coastal Waters*; Cambridge University Press: Cambridge, UK, 2010.

40. Longuet-Higgins, M.S. The directional spectrum of ocean waves, and processes of wave generation. *Proc. R. Soc. London. Ser. A. Math. Phys. Sci.* **1962**, *265*, 286–315.

41. He, K.; Zhang, X.; Ren, S.; Sun, J. Deep residual learning for image recognition. In Proceedings of the IEEE Computer Society Conference on Computer Vision and Pattern Recognition (CVPR), Las Vegas, NV, USA, 27–30 June 2016; pp. 770–778.

42. Alpers, W.R.; Ross, D.B.; Rufenach, C.L. On the detectability of ocean surface waves by real and synthetic aperture radar. *J. Geophys. Res.* **1981**, *86*, 6481–6498. [CrossRef]

43. Ziemer, F.; Rosenthal, W. On the transfer function of a shipborne radar for imaging ocean waves. In Proceedings of the IEEE International Geoscience and Remote Sensing Symposium, Ann Arbor, MI, USA, 18–21 May 1987; pp. 1559–1564.

44. Fucile, F.; Ludeno, G.; Serafino, F.; Bulian, G.; Soldovieri, F.; Lugni, C. Some Challenges in Recovering Wave Features from a Wave Radar System. In Proceedings of the 26th International Ocean and Polar Engineering Conference, Rhodes, Greece, 26 June–21 July 2016.

45. Zinchenko, V.; Vasilyev, L.; Halstensen, S.O.; Liu, Y. An improved algorithm for phase-resolved sea surface reconstruction from X-band marine radar images. *J. Ocean Eng. Mar. Energy* **2021**, *7*, 97–114. [CrossRef]

46. Naaijen, P.; Wijaya, A.P. Phase Resolved Wave Prediction from Synthetic Radar Images. In Proceedings of the ASME 2014 33rd International Conference on Ocean, Offshore and Arctic Engineering, San Francisco, CA, USA, 8–13 June 2014.

47. Ludeno, G.; Brandini, C.; Lugni, C.; Arturi, D.; Natale, A.; Soldovieri, F.; Gozzini, B.; Serafino, F. Remocean System for the Detection of the Reflected Waves from the Costa Concordia Ship Wreck. *IEEE J. Sel. Top. Appl. Earth Obs. Remote Sens.* **2014**, *7*, 3011–3018. [CrossRef]